Available online at www.sciencedirect.com
ScienceDirect
Trans. Nonferrous Met. Soc. China 35(2025) 819−831
Transactions of Nonferrous Metals Society of China
www.tnmsc.cn

Simultaneous enhancement of strength and thermal conductivity of extruded Mg−Mn−Zn alloy via hot compression

Hai-feng LIU[1], Xu-yue YANG[1], Yu-xiu ZHANG[1],
Hiromi NAGAUMI[2], Ming-chun ZHAO[1], Zhi-yong SHI[1], Andrej ATRENS[3]

1. School of Materials Science and Engineering, Central South University, Changsha 410083, China;
2. School of Iron and Steel, Soochow University, Suzhou 215100, China;
3. School of Mechanical & Mining Engineering, University of Queensland, Brisbane QLD4072, Australia

Received 30 July 2023; accepted 2 February 2024

Abstract: An additional hot compression process was applied to a dilute Mg−Mn−Zn alloy post-extrusion. The alloy was extruded at 150 °C with an extrusion ratio of 15:1 and subsequently hot-compressed at 180 °C with a true strain of 0.9 along the extrusion direction. The microstructure, mechanical properties and thermal conductivity of as-extruded and as-hot compressed Mg−Mn−Zn alloys were investigated using optical microscopy, scanning electron microscopy, electron backscattering diffraction, and transmission electron microscopy. The aim was to concurrently enhance both strength and thermal conductivity by fostering uniform and refined microstructures while mitigating basal texture intensity. Substantial improvements were observed in yield strength (YS), ultimate tensile strength (UTS), and elongation (EL), with increase of 77%, 53% and 10%, respectively. Additionally, thermal conductivity demonstrated a notable enhancement, rising from 111 to 125 W/(m·K). The underlying mechanism driving these improvements through the supplementary hot compression step was thoroughly elucidated. This study presents a promising pathway for the advancement of Mg alloys characterized by superior thermal and mechanical properties.
Key words: Mg alloys; hot compression; strength; thermal conductivity

1 Introduction

The industrial significance of thermal conductivity in Mg alloys is underscored by their widespread utilization as thermally conductive structural components across various sectors including automotive manufacturing, aerospace, and the 3C (computer, communication, and consumer electronics) industry [1,2]. Typically, there are specified requirements for thermal conductivity at room temperature (RT), with values exceeding 100 W/(m·K) for as-cast Mg alloys and 120 W/(m·K) for wrought Mg alloys [3]. Furthermore, structural components necessitate not only thermal properties but also mechanical strength, such as the shell of automobile engines, the radiator structure of electric equipment, and the radiating module of light-emitting diodes (LEDs) [4]. Pure Mg exhibits commendable RT thermal conductivity (156 W/(m·K)), second only to pure Al (237 W/(m·K)) among commercially-used metallic materials for these applications [5]. Particularly, Mg boasts a lower density and higher specific heat capacity compared to pure Al, making it a compelling candidate for heat dissipation materials, given the requirement for lightweight and efficient heat dispersion capabilities [6]. Pure Mg possesses low strength (~21 MPa for cast Mg) [5] and alloying has been thus widely used to increase the mechanical

Corresponding author: Ming-chun ZHAO, Tel/Fax: +86-731-88830830, E-mail: mczhao@csu.edu.cn
DOI: https://doi.org/10.1016/S1003-6326(24)66716-6

properties of Mg [7]. However, alloying typically leads to a reduction in thermal conductivity due to the formation of precipitates and/or lattice distortion caused by alloying elements [8]. Achieving a balance between strength and thermal conductivity is challenging due to conflicting operative mechanisms. Various alloying elements exhibit diverse effects on the mechanical properties and thermal performance of Mg alloys [3,5,9,10], necessitating careful selection of alloying element type and concentration to attain an optimal balance between thermal and mechanical properties [3,9]. While chemical composition optimization may not suffice to increase the thermal conductivity of an alloy to that of pure Mg, it can meet the critical required values [3].

So far, low-alloyed Mg−Mn−Zn series alloys have emerged as promising candidates for applications in thermally conductive structural components. The addition of Zn as an alloying element elicits a significant response in terms of precipitation hardening and strengthening, while Mn improves heat resistance and refines grain size in resulting Mg alloys [11,12]. YUAN et al [11], PENG et al [13], and FANG et al [14] have reported that the thermal conductivity of as-cast Mg−Zn−Mn series alloys surpasses the critical value required for cast Mg alloys utilized in heat dissipation applications. Additionally, PENG et al [3] further demonstrated that as-extruded Mg−Zn−Mn series alloys exhibit higher thermal conductivity and strength compared to their as-cast counterparts. However, the quest for improved material properties continues, with studies indicating that hot compression holds significant potential for microstructure modification and property enhancement in extruded Mg alloys [14−16]. Incorporating hot compression could prove to be an effective strategy for enhancing the properties of extruded Mg alloys.

To date, hot compression has not been utilized to enhance the mechanical properties and thermal conductivity of extruded Mg−Mn−Zn series alloys. To address this issue, in this study, Mg−1.0Mn−0.8Zn (wt.%) alloy was employed as the starting material, aiming to improve its mechanical properties and thermal conductivity through extrusion followed by hot compression. This research endeavor is expected to contribute significantly to the development of high-performance Mg alloys with superior thermal and mechanical properties.

2 Experimental

The Mg−1.0Mn−0.8Zn alloy underwent a melting process in an electronic resistance furnace, combining high-purity Mg (99.99 wt.%), Mg−6.4wt.%Mn master alloy, and high-purity Zn (99.99 wt.%), at 700 °C under a protective atmosphere of CO_2 and SF_6. The chemical composition (mass fraction, %) of the alloy, comprising 0.99% Mn, 0.83% Zn, and the balance of Mg, was determined using a SPECTROMAXx direct reading spectrometer. To achieve homogeneity, eliminate coarse intermetallic compounds, and ensure successful extrusion, the cast alloy ingot underwent a soaking process at 430 °C for 20 h. Extrusion was carried out at 150 °C with an extrusion ratio of 16:1 and a speed of 0.1 mm/s, resulting in an as-extruded bar with a diameter of 30 mm. Blanks, measuring 20 mm in diameter and 25 mm in height, were machined from the as-extruded bar and compressed at 180 °C with a strain rate of 3.0×10^{-3} s^{-1} and a true strain of 0.9 along the extrusion direction (ED), as depicted in Fig. 1 using an Instron-type mechanical testing machine. Subsequently, the samples were quenched in water to room temperature. Graphite powder was used as lubricant to minimize friction during the hot compression process. The resulting samples from extrusion alone were labeled as AE samples, while those from both extrusion and compression were termed AC samples in this study.

The microstructural analysis employed a comprehensive suite of techniques including optical microscopy (OM), scanning electron microscopy

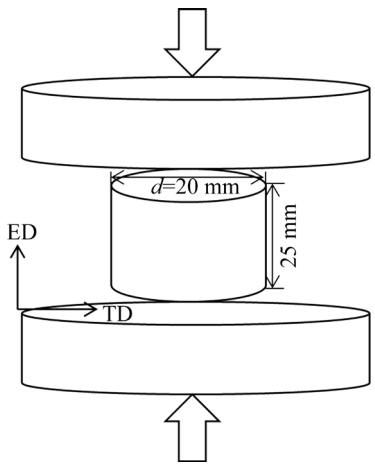

Fig. 1 Schematic diagram of hot compression

(SEM), electron backscattering diffraction (EBSD), and transmission electron microscopy (TEM). Specimens designated for OM and SEM underwent preparation via conventional mechanical techniques. EBSD specimens preparation involved initial mechanical grinding followed by electrolytic polishing with a nitric acid solution (1 mL nitric acid + 10 mL ethanol) under specific conditions including an electrolysis voltage of approximately 20 V, a current ranging between 0.10 and 0.15 A, and conducted within a low-temperature environment facilitated by liquid nitrogen (−40 °C to 30 °C) for approximately 1 min. Analysis of EBSD data, including grain size, pole and inverse pole figures, and kernel misorientation angle information was performed by TSL-OIM software.

Tensile specimens with dimensions of 6 mm (length) × 3 mm (width) × 1 mm (thickness) were machined from the central region of AE and AC blanks. All specimens were aligned with the transverse direction (TD), as illustrated in Fig. 2(a), for subsequent uniaxial tensile testing. These tests were conducted utilizing an Instron-type mechanical testing machine, applying a strain rate of $3.0\times10^{-3}\ s^{-1}$ at room temperature (RT). Density measurements were carried out employing the Archimedes principle method, utilizing a JA3003 electronic analytical balance [17]. Thermal conductivity evaluations were performed along the TD at RT, employing an LFA457/2/G thermal conductivity analyzer. Machined disks with a diameter of 10 mm and a thickness of 2 mm were utilized, as schematically represented in Fig. 2(b). Prior to the commencement of thermal conductivity testing, the oxide layers present on the upper and lower surfaces were meticulously removed using 4000# water-grid sandpaper. Subsequently, a uniform layer of graphite was applied to the top surface to enhance light absorption. Each test was repeated three times to ensure accuracy and obtain an average value.

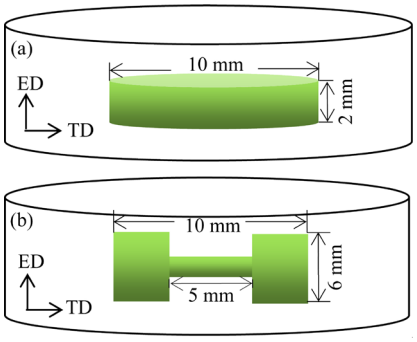

Fig. 2 Specimens for tensile (a) and thermal conductivity (b) tests

3 Results

3.1 Microstructures

Figure 3 shows optical micrographs of the AE sample (Fig. 3(a)) and the AC sample (Fig. 3(b)) which show a mixed microstructure of ultra-fine dynamic recrystallized (DRXed) grains and coarse non-dynamic recrystallized (non-DRXed) grains. This mixed microstructure was attributed to incomplete dynamic recrystallization during the low-temperature extrusion. There was a pronounced microstructural distinction between the AE and AC samples. Compared with the AE sample, the AC sample had a higher volume fraction of the recrystallization grains, which indicated that the hot compression following the low-temperature extrusion promoted the occurrence of the recrystallization for those non-DRXed grains in the AE sample.

In Fig. 4, the EBSD data of the AE sample are depicted, with the observation direction aligned parallel to the ED. Grain boundaries, as depicted in Fig. 4(a), clearly reveal a bimodal-sized microstructure post low-temperature extrusion, wherein

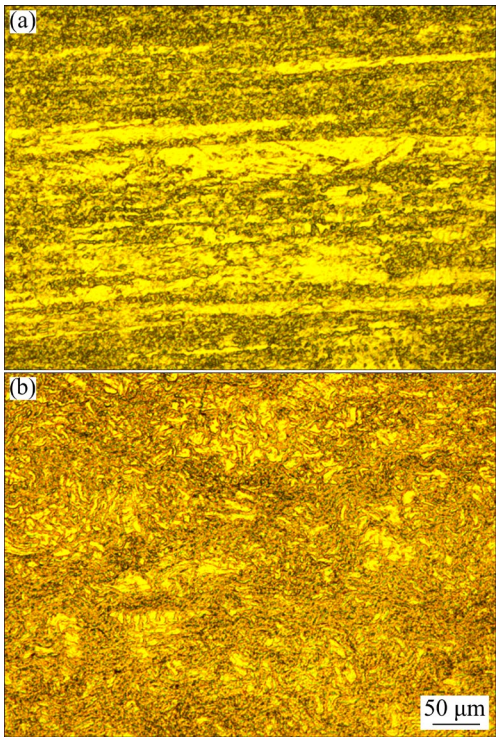

Fig. 3 Optical micrographs of AE (a) and AC (b) samples

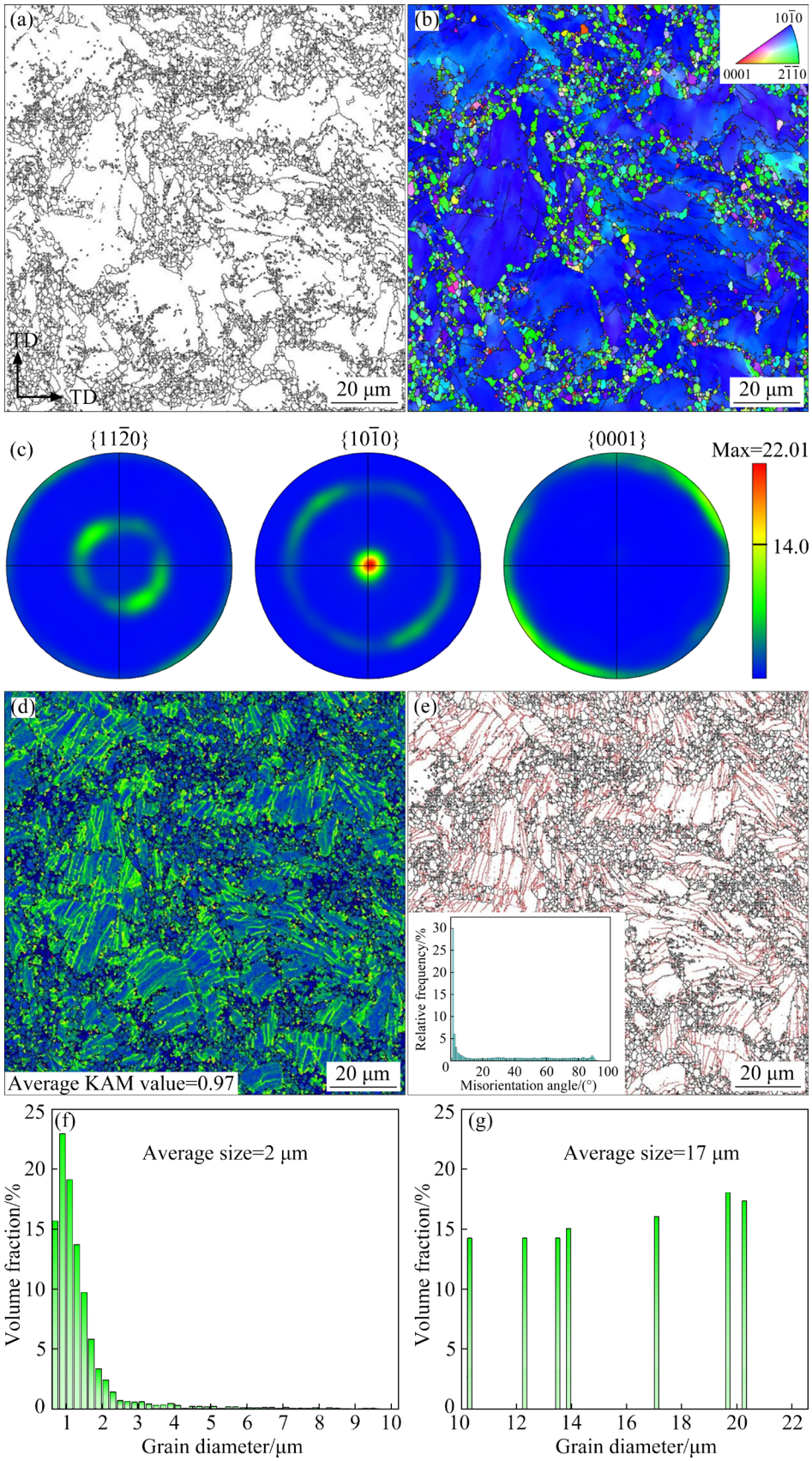

Fig. 4 Grain boundaries map of AE sample (a), typical IPF map (b), corresponding {11$\bar{2}$0}, {10$\bar{1}$0} and {0001} pole figures (c), KAM map (d), grain boundary and misorientation distribution maps (e), size distribution of non-DRXed grains (f), and size distribution of DRXed grains (g)

the finer grains correspond to dynamically recrystallized (DRXed) grains, while the coarser grains correspond to non-dynamically recrystallized (non-DRXed) grains. This observation is consistent with the metallographic characteristics presented in Fig. 3(a). The inverse pole figure (IPF) shown in Fig. 4(b) illustrates that all grains exhibit a blue or green color, indicative of a typical extruded texture with basal planes oriented parallel to the ED. Figure 4(c) presents the texture in the form of pole figures, wherein the pole figures are distributed in across the corresponding $\{11\bar{2}0\}$, $\{10\bar{1}0\}$, and $\{0001\}$ pole figures. Notably, pole intensity of the $\{10\bar{1}0\}$ texture is centrally located with a texture intensity of 22, whereas $\{0001\}$ pole figures are concentrated at the periphery with a texture intensity of 14, affirming an extremely strong texture following the low-temperature extrusion. Figure 4(d) shows a typical kernel average misorientation (KAM) map, revealing local misorientation and strain energy. The green areas within the KAM map signify lattice strain induced by a high dislocation density. While significant lattice strain induced by the high dislocation density persists in the coarser non-DRXed grains, no traces of stress concentration are observed in the DRXed grains. Figure 4(e) provides insight into grain boundaries and misorientation distribution. High-angle grain boundaries (HAGBs), delineated by black lines, and low-angle grain boundaries (LAGBs), depicted by red lines, are discernible. The concentration of LAGB primarily within the non-DRXed grains suggests their retention as such due to their status as hard orientation regions and the absence of recrystallization driving force. The accompanying misorientation angle distribution maps indicates a volume fraction of LAGB at 52%, with the largest volume fraction occurring at a misorientation of approximately 1.5°, reaching 30%. Figures 4(f, g) present the size distribution of non-DRXed and DRXed grains, respectively. The volume fractions of DRXed and non-DRXed grains stand at 55% and 45%, respectively. Furthermore, the average sizes of DRXed and non-DRXed grains are approximately 2 and 17 μm, respectively.

In Fig. 5, the EBSD data corresponding to the AC sample are presented. Grain boundaries depicted in Fig. 5(a) reveal a relatively homogeneous microstructure, distinct from that of the AE sample in Fig. 4(a). This indicates that the AC sample predominantly experienced complete dynamic recrystallization. The inverse pole figure (IPF) illustrated in Fig. 5(b) shows all grains adorned with the red color, signifying a significant alteration in grain orientation from the AE sample, wherein basal planes have rotated from the ED to the TD. Figure 5(c) delineates the texture through polar maps. A more dispersed pole distribution is observed in the AE sample across all pole maps compared to the AC sample. Additionally, the basal texture intensity experiences a drastic reduction to 7, which is attributed to the random orientation of new grains formed during dynamic recrystallization. Figure 5(d) depicts a typical KAM map. A sharp decrease in the green area within the KAM map indicates a reduction in lattice strain induced by high dislocation density, validating the dynamic recrystallization of coarse non-DRXed grains with high stored energy induced by hot compression. Figure 5(e) shows the misorientation distribution maps. Compared to the AE sample, the AC sample exhibits a decreased volume fraction of LAGBs and an increased volume fraction of HAGBs. This transition from LAGBs to HAGBs provides clear evidence of dynamic recrystallization occurrence. The size distribution of DRXed grains is presented in Fig. 5(f), with an average size of approximately 2.1 μm. Notably, given the slightly higher temperature during hot compression compared to extrusion, the DRXed grains in the AE sample experience slight growth during subsequent hot compression.

In Fig. 6, representative SEM micrographs exhibit the AE and AC samples, both featuring precipitates. Notably, the AC sample displays a higher density of precipitates compared to the AE sample, suggesting the formation of precipitates from the Mg matrix during hot compression. Figure 7 presents representative TEM micrographs of the AE and AC samples. In the AE sample, the formation of twins is evident, with the twinning boundaries effectively trapping dislocations, as depicted in Fig. 7(a). This twinning behavior serves to alleviate strain along the *c*-axis of the Mg alloy during low-temperature deformation, consequently enhancing mechanical properties by impeding dislocation motion [18]. Furthermore, the disappearance of twins in the AC sample, as shown

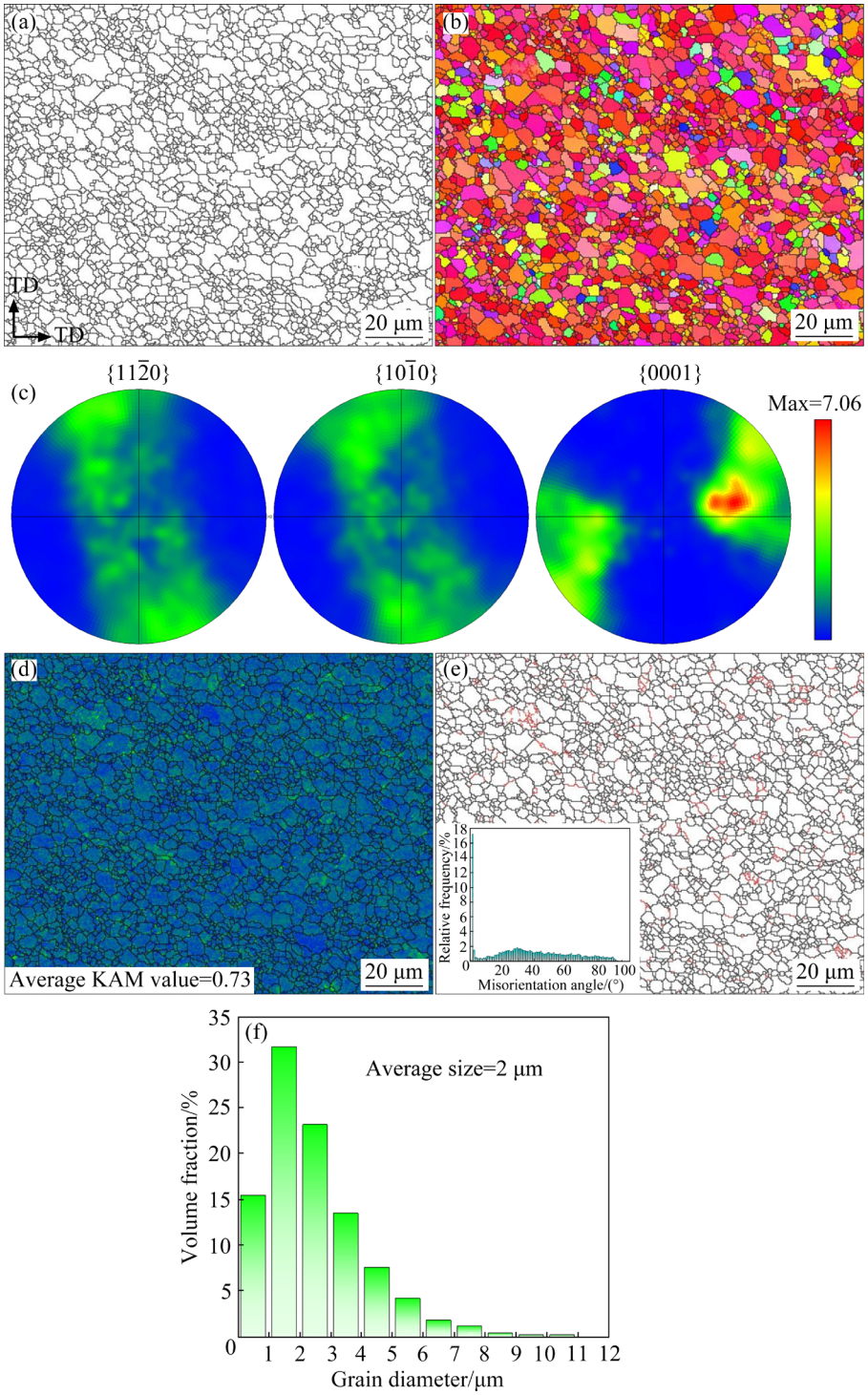

Fig. 5 Grain boundaries map of AC sample (a), typical IPF map (b), corresponding {11$\bar{2}$0}, {10$\bar{1}$0} and {0001} pole figures (c), KAM map (d), characterized grain boundaries and misorientation distribution (e), and size distribution of DRXed grains (f)

in Fig. 7(b), is observed. Additionally, the AC sample exhibits a higher density of nano-precipitates compared to the AE sample. This underscores that hot compression facilitates the dynamic precipitation of nano-precipitates, aligning with SEM observations.

In Fig. 8, high-angle annular dark field scanning transmission electron microscopy (HAADF-STEM) images reveal distinct micro-structural features in the AE and AC samples. For the AE sample (Figs. 8(a−d)), solely nanoscale α-Mn particles are evident. These particles are

believed to originate from the fragmentation of α-Mn particles during extrusion, forming through a crushing mechanism. Conversely, in the AC sample (Figs. 8(e−h)), short rod-like precipitates containing Mn are observed. These precipitates are attributed to the dynamic precipitation of Mn from the Mg matrix during hot compression. Furthermore, nano-Zn-containing precipitates are also present in the AC sample, formed during hot compression [19]. These nanoscale MgZn2 precipitates, ubiquitously present in Mg−Zn alloys, act as primary strengthening phases by impeding [20].

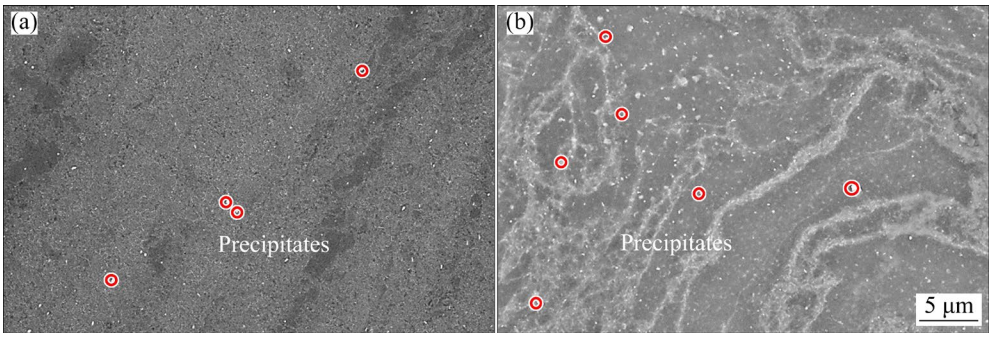

Fig. 6 SEM micrographs of AE sample (a) and AC sample (b)

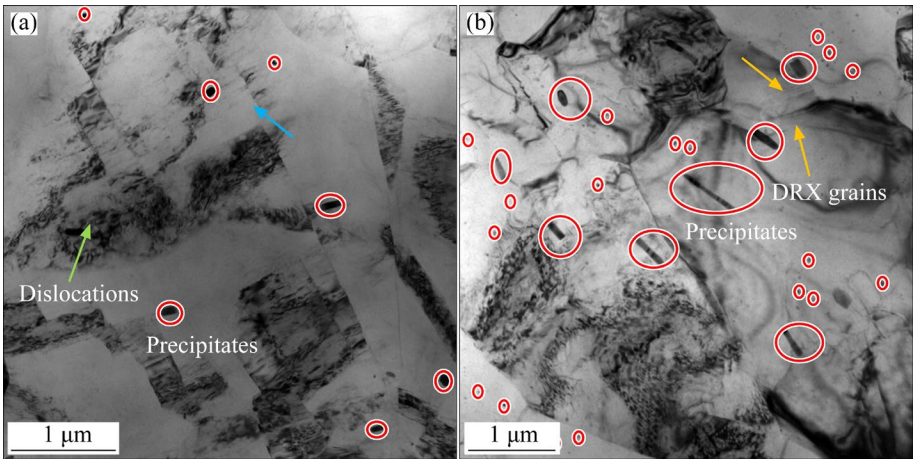

Fig. 7 TEM micrographs of AE sample (a) and AC sample (b)

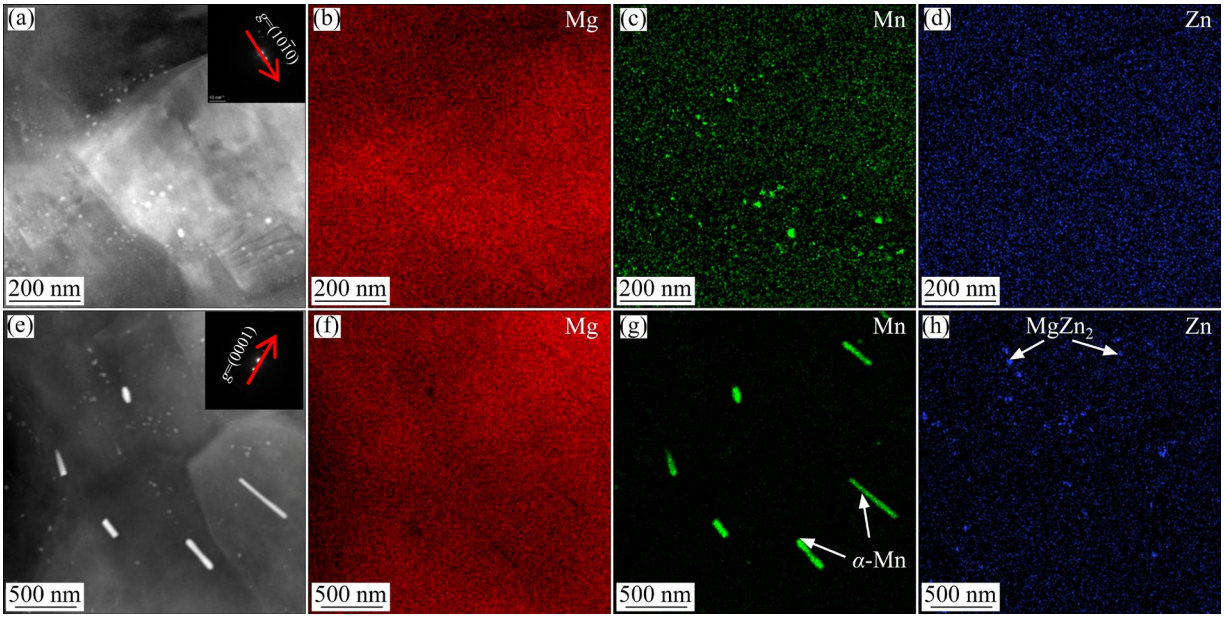

Fig. 8 HAADF-STEM images with incident beam direction of $\boldsymbol{B}=[2\bar{1}\bar{1}0]$ and distribution of Mg, Mn and Zn elements: (a−d) AE sample; (e−h) AC sample

3.2 Uniaxial tensile properties

Figure 9 presents the uniaxial tensile curves of the AE and AC samples, offering insights into the impact of hot compression on the mechanical properties of the low-temperature extruded Mg−1.0Mn−0.8Zn alloy. In the AE sample, the yield strength (YS), ultimate tensile strength (UTS), and fracture elongation (EL) were measured to be (162±3) MPa, (202±4) MPa and (10.1±1)%, respectively. Comparatively, the AC sample exhibits higher values across all parameters, with YS, UTS, and EL reaching (287±4) MPa, (308±5) MPa, and (11.1±1)%, respectively. Notably, the AC sample demonstrates a substantial improvement, with YS, UTS, and EL increasing by 77%, 53%, and 10%, respectively, compared to the AE sample.

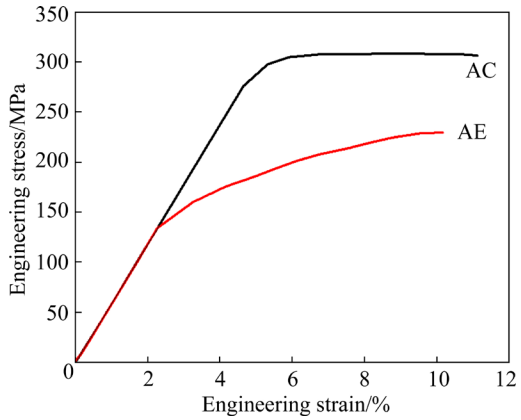

Fig. 9 Engineering stress−strain curves at room temperature

Figure 10 illustrates the room temperature (RT) tensile fracture morphology of the AE and AC samples. The fracture surfaces of the AE sample, depicted in Fig. 10(a), display smooth cleavage facets, indicative of a fracture mechanism predominantly characterized by brittle fracture, supplemented by some ductile fracture. Additionally, the presence of secondary cracks in Fig. 10(a) suggests local stress concentration. In contrast, the fracture surfaces of the AC sample, as shown in Fig. 10(b), exhibit an increase in the number of dimples and a decrease in the number of cleavage surfaces. This observation signifies a transition towards ductile fracture as the dominant mechanism in the AC sample. The difference in fracture morphology between the AE and AC samples accurately reflects the observed mechanical property results.

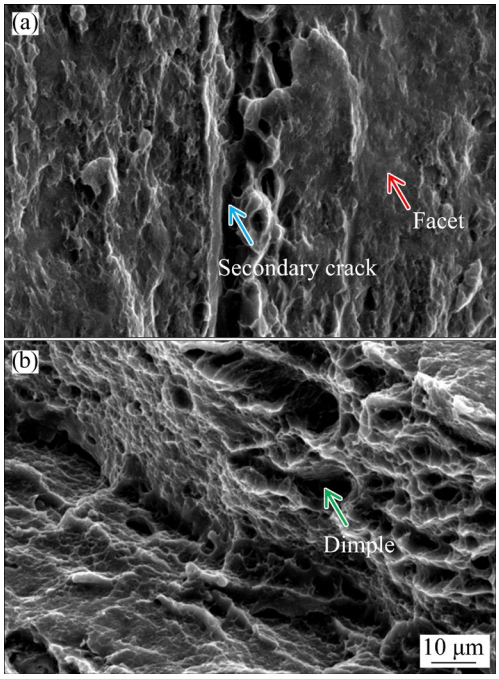

Fig. 10 Tensile fracture morphology of AE sample (a) and AC sample (b)

3.3 Thermal conductivity

Table 1 lists the thermal conductivity of the AE and AC samples, which were calculated using the following equation:

$$\lambda=\alpha C\rho \quad (1)$$

where λ is the thermal conductivity, α is the thermal diffusion coefficient, C is the specific heat capacity, and ρ is the material density. The AC sample had higher thermal conductivity than the AE sample, which were ~125 and 111 W/(m·K), respectively. These two samples had much higher thermal conductivity than the common Mg−RE-based and Mg−Al-based alloys, whose thermal conductivity

Table 1 Thermal diffusion coefficient and thermal conductivity of AE and AC samples at room temperature

Sample	Thermal diffusivity/ (10^{-4} mm^2·s^{-1})	Thermal conductivity/ (W·m^{-1}·K^{-1})	Average of thermal conductivity/ (W·m^{-1}·K^{-1})
AE	65	113	111
	63	109	
	64	111	
AC	72	125	~125
	72	125	
	72	124	

was usually lower than 100W/(m·K). This indicates that the Mg−Mn−Zn-based alloys have great potential for developing into a high thermal conductivity material.

4 Discussion

4.1 Strengthening mechanism

The tensile results show that the strength of the AE sample is significantly improved by the subsequent hot compression treatment. The strength of the alloy can be attributed to the solid solution strengthening, grain boundary strengthening, precipitation strengthening and texture strengthening, which can be described as [21]

$$\sigma_y=\sigma_{gb}+\sigma_{ss}+\sigma_{ps}+\sigma_{ts} \quad (2)$$

where σ_y is the yield strength increment, σ_{gb} is the contribution of grain boundary strengthening, σ_{ss} is the contribution of solution strengthening, σ_{ps} is the contribution of precipitation strengthening, and σ_{ts} is the contribution of texture strengthening.

(1) Hot compression following extrusion imposed a great grain refinement effect on the present alloy. The estimated σ_{gb} increment could be calculated following the Hall−Petch relation [21,22]:

$$\sigma_{gb}=kd^{-1/2} \quad (3)$$

where k is 273 MPa/μm$^{-1/2}$ for Mg alloys, and d is the average grain size [23,24]. As stated before, the AE sample presented a distinct bimodal-sized microstructure containing both ultra-fine DRXed grains and coarse non-DRXed grains. Therefore, the estimated σ_{gb} increment could be evaluated using the following equation:

$$\sigma_{gb}=kd_{AC}^{-1/2}-k(f_{DRX-AE}d_{DRX-AE}^{-1/2}+f_{non\text{-}DRX-AE}d_{non\text{-}DRX-AE}^{-1/2}) \quad (4)$$

where d_{AC} is the average grain size of the AC sample, which is 2.1 μm; f_{DRX-AE} and $f_{non\text{-}DRX-AE}$ are the volume fractions of the DRXed grains and the non-DRXed grains of the AE sample, which were 55.3% and 44.7%, respectively; d_{DRX-AE} and $d_{non\text{-}DRX-AE}$ are the average grain size in the DRXed and non-DRXed region in the AE sample, which were 2 and 17 μm, respectively. As a result, the yield strength increment by grain boundary strengthening was calculated to be ~52 MPa.

(2) Since the solid solubility of Mn in Mg matrix is almost zero at RT, the solid solution strengthening of Mn on Mg−Mn−Zn alloy might be neglected. The solid solution strengthening of Zn solute atoms on Mg matrix can be calculated using the following equation:

$$\sigma_{SS}=k_{Zn}c_{Zn}^{n} \quad (5)$$

where k_{Zn} (905 MPa·at.%$^{-2/3}$) is a factor associated with Zn solute atoms, c_{Zn} is the solute atomic concentration, respectively, and n is a constant equal to 2/3. Substituting the above-given data, the yield strength reduction by the solid strengthening was calculated to be ~10 MPa.

(3) For precipitation strengthening to be effective, the particle size must be very small. The critical radius from the shearing mechanism to the bypass mechanism of the precipitates is about a few nanometers [25]. As the particle size surpasses this critical radius, the strengthening effect diminishes. In the AC sample, the short rod-like α-Mn precipitates were observed to be at the micron level, considerably larger than the critical radius. Consequently, the strengthening effect attributed to precipitation strengthening from these precipitates in the AC sample was likely negligible. On the other hand, the existence of a large amount of nanoscale precipitates made a significant contribution to precipitation strengthening. Furthermore, these nanoscale precipitations were hard and resistant to dislocation shear. Instead, dislocations tended to bypass rather than shear them, resulting in bypass strengthening, also known as Orowan strengthening. The Orowan strengthening effect can be described by the following formula [26]:

$$\sigma_{ps}=M\frac{Gb}{2\pi\sqrt{1-v}}\frac{1}{\sqrt{\frac{2}{3}}d_p\left(\sqrt{\frac{\pi}{4f_p}}-1\right)}\ln\frac{\sqrt{\frac{2}{3}}d_p}{b} \quad (6)$$

where M is the Taylor factor (2.5 for Mg alloys), v is the Poisson ratio (0.35 for Mg alloys), G is the shear modulus (16.6 GPa for Mg alloy), b is the component of Burger vector (0.32 nm for Mg alloys), d_p is the average particle size, and f_p is the volume fraction of the precipitations. Based on statistics from STEM (Fig. 8), the d_p and f_p were 10 nm and 2% for the AE sample while 9 nm and 3% for the AC sample, respectively. Substituting these values, the yield strength increment by the precipitation strengthening was calculated to be ~44 MPa. It is noteworthy that the nanoscale precipitations

distributed at the grain boundaries played a pegging role, hindering grain growth after dynamic recrystallization and enhancing the effect of fine grain strengthening [27].

(4) As mentioned earlier, the cyclic texture with the basal plane parallel to the extrusion direction (ED) was obtained after extrusion, while the room temperature tensile direction was parallel to the transverse direction (TD). Most grains in the AE sample are "softly oriented" with respect to basal slip, leading to a lower yield strength (YS). However, hot compression reoriented the basal plane of most grains from ED to TD. Consequently, in the AC sample, when tensile along the TD, the force axis direction paralleled the basal plane with the Schmid factor of the basal planes close to 0. This made basal slip difficult, resulting in texture reinforcement [28]. The contribution of texture strengthening could be calculated using the following equations [29]:

$$\sigma_{ts}=\sigma_{ts+gb}-\sigma_{gb} \quad (7)$$

$$\sigma_{ts+gb}=\sigma_{gb}(0.3/m) \quad (8)$$

where σ_{ts+gb} is the combined contribution of texture strengthening and grain boundary strengthening, and m is the average Smithian factor of the basal slip which is 0.2, and σ_{gb} was calculated as ~52 MPa as mentioned above. Consequently, the yield strength increment by texture strengthening is calculated to be approximately ~26 MPa.

At last, the overall strengthening exhibits an accumulation effect, with the total YS increment mainly attributed to the grain boundary strengthening increment (~52 MPa), precipitation strengthening increment (~44 MPa), and texture strengthening increment (~26 MPa), totaling 122 MPa, which is in good agreement with the experimentally measured value of the YS strengthening increment (125 MPa).

4.2 Effect of hot compression on thermal conductivity

Thermal conductivity in materials is notably influenced by microstructural factors such as texture, solute atoms, grain boundaries (GBs), and dislocations. These factors act as scattering centers for both electrons and phonons, diminishing their average free range and thereby reducing the thermal conductivity of material [13,30−32].

The impact of hot compression processing on the thermal conductivity of the alloy is multifaceted as: (1) The basal plane rotation from the extrusion direction (ED) to the transverse direction (TD) after hot compression alters the electron and phonon scattering behavior. This results in a decrease in thermal conductivity due to scattering from dense rows of atoms in the AC sample, especially when the measurement direction of thermal conductivity aligns with the TD. This effect has been demonstrated by YUAN et al [11] through investigation on the thermal conductivity of extruded Mg−5Mn−1Zn alloy. (2) Dynamic recrystallization during hot compression increases the volume fraction of grain boundaries in the AC sample [33]. Grain boundaries act as additional scattering centers for electrons and phonons, further reducing the thermal conductivity of the alloy. This phenomenon is supported by research, which indicates that the increased volume fraction of grain boundaries is a primary reason for the lower thermal conductivity of extruded samples compared with cast samples in Mg−Mn−Zn−Nd alloys [5]. Considering only these two factors would not fully explain the experimental results. Thus, other factors must counteract the negative effects of both basal plane deflection and increased grain boundary density on the thermal conductivity of alloys.

Solute atoms, functioning as impurities, play a crucial role. The substitution of Mg atoms by solute atoms alters the lattice constant and disrupts the periodicity of the Mg atomic array, significantly decreasing the thermal conductivity of the alloy [4]. Conversely, the presence of atoms in the form of a second phase, without modifying the crystal structure of the Mg matrix, has a negligible effect on thermal conductivity [1]. YING et al [34] reported that solid solution atoms with similar valence and volume as the Mg matrix cause less lattice distortion, consequently, have a smaller effect on thermal conductivity. However, Mn, with its unfavorable atomic size and valence, generates significant lattice distortion when solidly dissolved in the Mg matrix, leading to a dramatic drop in thermal conductivity of Mg−Mn−Zn alloys [35]. In contrast, Zn atoms had relatively small effect on the thermal conductivity [36,37]. During hot compression of the Mg−Mn−Zn alloy, dynamic precipitation of Mn and Zn atoms occurs more intensively in the AC sample. The precipitation mechanism diagram is shown in Fig. 11. Zn atoms

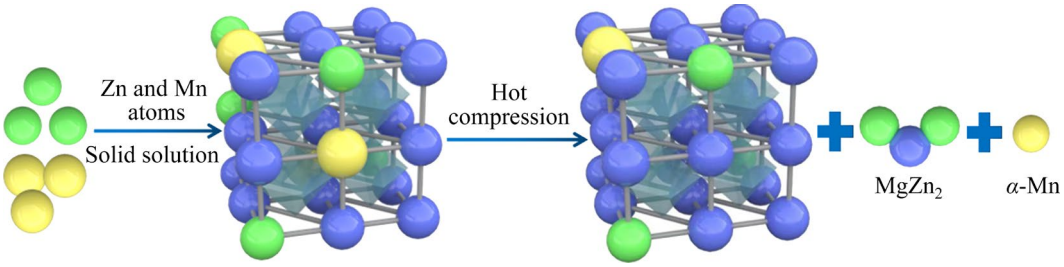

Fig. 11 Precipitation mechanism of second phase of Mg−Mn−Zn alloy promoted by hot compression

precipitate in the form of $MgZn_2$, while Mn atoms precipitate as α-Mn. This dynamic precipitation significantly reduces the degree of lattice distortion compared to solute atoms dissolved in the matrix. The relief of lattice distortion due to precipitation is supported by the decrease in the KAM value from 0.97 for the AE sample to 0.73 for the AC sample as shown in Figs. 4(d) and 5(d), respectively.

The combined influence of the aforementioned factors on the thermal conductivity of the Mg−Mn−Zn alloy exhibits contradictory trends. While texture evolution and increased grain boundary density tend to decrease thermal conductivity, the presence of solute atoms, particularly Mn and Zn, acts to alleviate this reduction. Among these factors, the dominance of the third factor, namely the dynamic precipitation of Mn and Zn atoms during hot compression, emerges as the primary determinant.

As a result, despite the potentially negative effects of texture evolution and increased grain boundary density, the dominant influence of dynamic precipitation leads to an overall improvement in the thermal conductivity of the alloy following hot compression.

5 Conclusions

(1) The AC samples exhibits a finer and more uniform microstructure with reduced texture intensity compared to the AE sample, indicating the efficacy of hot compression in promoting dynamic recrystallization.

(2) Yield strength, ultimate tensile strength, and elongation of the AC sample were enhanced by 77%, 53% and 10%, respectively, relative to the AE sample. This strengthening was attributed to the synergistic effects of grain boundary strengthening, precipitation phase strengthening, and texture strengthening.

(3) Thermal conductivity increases from 111 W/(m·K) in the AE sample to 125 W/(m·K) in the AC sample. The precipitation of Mn and Zn atoms counters the adverse effects of increased grain boundary volume and rotated texture during hot compression, resulting in an elevated thermal conductivity of the alloy.

(4) The concurrent improvement in strength and thermal conductivity of an extruded Mg−Mn−Zn dilute alloy via hot compression presents a promising avenue for the advancement of Mg alloys with superior thermal and mechanical properties.

CRediT authorship contribution statement

Hai-feng LIU: Conceptualization, Writing − Original draft, Review & editing, Formal analysis; **Xu-yue YANG:** Conceptualization, Supervision, Funding acquisition; **Yu-xiu ZHANG** and **Hiromi NAGAUMI:** Investigation; **Ming-chun ZHAO:** Conceptualization, Supervision, Funding acquisition; **Zhi-yong SHI** and **Andrej ATRENS**: Investigation.

Declaration of competing interest

The authors declare that they have no known competing financial interests or personal relationships that could have appeared to influence the work reported in this paper.

Data availability statement

All data included in this study are available upon request by contact with the corresponding author.

Acknowledgments

This work was financially supported by the National Key Research and Development Program of China (No. 2022YFE0109600), and the National Natural Science Foundation of China (No. 52150710544).

References

[1] CHEN Hong-can, XIE Tian-ci, LIU Quan, HUANG Yuan-ding, LIU Bin, LUO Qun, LI Qian. Mechanism and prediction of aging time related thermal conductivity evolution of Mg−Zn alloys [J]. Journal of Alloys and Compounds, 2023, 930: 167392.

[2] INOUE S I, ISHIAGE K, KAWAMURA Y. Optimization of heat treatment condition of nonflammable Mg−Al−Ca alloys with high thermal conductivity [J]. Journal of Alloys and Compounds, 2023, 934: 168014.

[3] PENG Jian, ZHONG Li-ping, WANG Yong-jian, LU Yun, PAN Fu-sheng. Effect of extrusion temperature on the microstructure and thermal conductivity of Mg−2.0Zn−1.0Mn−0.2Ce alloys [J]. Materials & Design, 2015, 87: 914−919.

[4] LI Zi-xin, HU Bo, LI De-jiang, ZHANG Wei-chen, ZENG Xiao-qin, LI Zhan-hong, JIN Chen, ZHAO Shou. Microstructure-dependent thermal conductivity and mechanical properties in cast Mg−4Sm−*x*Al alloys [J]. Materials Science and Engineering: A, 2022, 861: 144336.

[5] ZHOU Ying-long, LIU Jie, LUO Dong-mei, CHEN Dong-chu. Evaluation of the effect of Nd content and extrusion process on thermal conductivity of Mg−Mn−Zn−Nd alloys [J]. Crystals, 2018, 8: 427.

[6] ZHANG Li, DENG Kun-kun, NIE Kai-bo, WANG Cui-ju, XU Chao, SHI Quan-xin. Achieving strength-thermal conductivity synergy in Mg bulk system via introducing oriented graphite flakes into Mg−Zn−Ca alloy [J]. Composites Communications, 2023, 37: 101451.

[7] TAO Jun-xi, ZHAO Ming-chun, ZHAO Ying-chao, YIN Deng-feng, LIU Long, GAO Cheng-de, SHUAI Ci-jun, ATRENS A. Influence of graphene oxide (GO) on microstructure and biodegradation of ZK30-xGO composites prepared by selective laser melting [J]. Journal of Magnesium and Alloys, 2020, 8: 952−962.

[8] BAZHENOV V E, KOLTYGIN A V, SUNG M C, PARK S H, TSELOVALNIK Y V, STEPASHKIN A A, RIZHSKY A A, BELOV M V, BELOV V D, MALYUTIN K V. Development of Mg−Zn−Y−Zr casting magnesium alloy with high thermal conductivity [J]. Journal of Magnesium and Alloys, 2021, 9: 1567−1577.

[9] RUDAJEVOVÁ A, LUKÁČ P. Comparison of the thermal properties of AM20 and AS21 magnesium alloys [J]. Materials Science and Engineering: A, 2005, 397: 16−21.

[10] ZHAO Ming-chun, DENG Yun-lai, ZHANG Xin-ming. Strengthening and improvement of ductility without loss of corrosion performance in a magnesium alloy by homogenizing annealing [J]. Scripta Materialia, 2008, 58: 560−563.

[11] YUAN Jia-wei, ZHANG Kui, LI Ting, LI Xing-gang, LI Yong-jun, MA Ming-long, LUO Ping, LUO Guang-qiu, HAO Yong-hui. Anisotropy of thermal conductivity and mechanical properties in Mg−5Zn−1Mn alloy [J]. Materials & Design, 2012, 40: 257−261.

[12] XIE Bin, ZHAO Ming-chun, XU Rong, ZHAO Ying-chao, YIN Deng-feng, GAO Cheng-de, ATRENS A. Biodegradation, antibacterial performance, and cyto-compatibility of a novel ZK30-Cu−Mn biomedical alloy produced by selective laser melting [J]. International Journal of Bioprinting, 2021, 7: 78−89.

[13] PENG Jian-zhong, LI ping, WANG Yong-jian, YANG Jiang, LU Yun, PAN Fu-sheng. Effect of Ce addition on thermal conductivity of Mg−2Zn−1Mn alloy [J]. Journal of Alloys and Compounds, 2015, 639: 556−562.

[14] FANG Zheng-wu, HUO Qing-huan, WANG Jing, XIAO Zhen-yu, ZHANG Du-xiu, HUANG Wei-ying, ZHAO Ming-chun, YANG Xu-yue. Creep behaviors of hot compressed Mg−4Y−2Nd−0.2Zn−0.5Zr alloy with and without aging [J]. Materials Science and Engineering: A, 2017, 708: 460−468.

[15] ZHANG Du-xiu, YANG Xu-yue, SUN Huan, LI Yi, WANG Jun, ZHANG Zhi-rou, YE You-xiong, SAKAI Ta-ku. Dynamic recrystallization behaviors and the resultant mechanical properties of a Mg−Y−Nd−Zr alloy during hot compression after aging [J]. Materials Science and Engineering: A, 2015, 640: 51−60.

[16] ZHANG Yu-xiu, CHEN Dong-liang, NAGAUMI H, YANG Xu-yue. Highly improved creep resistance of hot-extruded Mg−0.9Mn−0.5Ce alloy by conventional forging [J]. Materials Science and Engineering: A, 2022, 857: 144083.

[17] ZHAO Hui, ZHANG Li-tong, CHEN Bo, ZHANG Jia-xin. The effect of fiber orientation on failure behavior of 3DN C/SiC torque tube [J]. Ceramics International, 2018, 44: 4190−4197.

[18] ZHANG Zhi, ZHANG Jing-huai, XIE Jin-shu, LIU Shu-juan, FU Wei, WU Rui-zhi. Developing a Mg alloy with ultrahigh room temperature ductility via grain boundary segregation and activation of non-basal slips [J]. International Journal of Plasticity, 2023, 162: 103548.

[19] CAI Chang-hong, SONG Ren-bo, PENG Shi-guang, WANG Yong-jin, LI Jing-yuan. Microstructure, mechanical properties and tribological behavior of a novel low-alloy high strength Mg−2Zn−0.5Zr−0.5Nd alloy [J]. Vacuum, 2020, 179: 109518.

[20] BENDO A, MATSUDA K, LERVIK A, TSURU T, NISHIMURA K, NUNOMURA N, HOLMESTAD R, MARIOARA C D, SHIMIZU K, TODA H, YAMAGUCHI M. An unreported precipitate orientation relationship in Al−Zn−Mg based alloys [J]. Materials Characterization, 2019, 158: 109958.

[21] XIE Jin-shu, ZHANG Zhi, LIU Shu-juan, ZHANG Jing-huai, WANG Jun, HE Yu-ying, LU Li-wei, JIAO Yun-lei, WU Rui-zhi. Designing new low alloyed Mg−RE alloys with high strength and ductility via high-speed extrusion [J]. International Journal of Minerals, Metallurgy and Materials, 2023, 30: 82−91.

[22] ZHANG Wen, ZHAO Ming-chun, WANG Zhen-bo, TAN Li-li, QI Ying-wei, YIN Deng-feng, YANG Ke, ATRENS A. Enhanced initial biodegradation resistance of the biomedical Mg−Cu alloy by surface nanomodification [J]. Journal of Magnesium and Alloys, 2023, 11: 2776−2788.

[23] ZHANG Yu, ZHANG Ke, LIU Wei-dong, ZHENG Zhong-ren, ZHAO Ming-chun. Grain growth upon annealing and its influence on biodegradation rate for pure iron [J]. Materials, 2022, 15: 8030.

[24] YU Hui-hui, XIN Yun-chang, WANG Mao-yin, LIU Qing. Hall−Petch relationship in Mg alloys: A review [J]. Journal of Materials Science & Technology, 2018, 34: 248−256.

[25] ZHANG Shen-chen, YAO Jian-gang, WANG Ping, WANG Hua, ZHANG Ji-mou, YIN Deng-feng, ZHAO Ming-chun, ATRENS A. Formation of the primary second phases and their influence on the mechanical properties of an as-cast Al−Li−Mg alloy with multi-microalloying (Sc, Zr, Er and Ti) [J]. International Journal of Metalcasting, 2024, 18: 608−619.

[26] WEI Zhen, DONG Hao, ZHANG Jing-huai, WU Rui-zhi, HE Yu-ying, BAO Ri-rong, ZHANG Xiao-bo, WANG Jia-hao. Preparation of high strength Mg−Li−Zn−Y alloy by $MgLi_2Zn$ precipitation [J]. Materials Science and Engineering: A, 2024, 890: 145842.

[27] ZHAO Ying-chao, TANG Yue, ZHAO Ming-chun, LIU Long, GAO Cheng-de, SHUAI Ci-jun, ZENG Rong-chang, ATRENS A, LIN Yong-cheng. Graphene oxide reinforced iron matrix composite with enhanced biodegradation rate prepared by selective laser melting [J]. Advanced Engineering Materials, 2019, 21: 1900314.

[28] ZHANG Wen, TAN Li-li, NI Ding-rui, CHEN Jun-xiu, ZHAO Ying-chao, LIU Long, SHUAI Ci-jun, YANG Ke, ATEENS A, ZHAO Ming-chun. Effect of grain refinement and crystallographic texture produced by friction stir processing on the biodegradation behavior of a Mg−Nd−Zn alloy [J]. Journal of Materials Science and Technology, 2019, 35: 777−783.

[29] LI Guo-qiang, ZHANG Jing-huai, WU Rui-zhi, LIU Shu-juan, SONG Bo, JIAO Yu-feng, YANG Qiang, HOU Le-gan. Improving age hardening response and mechanical properties of a new Mg-RE alloy via simple pre-cold rolling [J]. Journal of Alloys and Compounds, 2019, 777: 1375−1385.

[30] YING Tao, ZHENG Ming-yi, LI Zi-tong, QIAO Xiao-guang, XU Shi-wei. Thermal conductivity of as-cast and as-extruded binary Mg−Zn alloys [J]. Journal of Alloys and Compounds, 2015, 621: 250−255.

[31] LI Xiang, LI Hong-ying, TANG Hao-qing, XIAO Xiang, HAN Jia-qiang, ZHENG Zi-qiao. Microstructure evolution and in situ resistivity response of 2196 Al−Li alloy during aging process [J]. Materials, 2023, 16: 7492.

[32] ZHANG Ai-ling, LI Yan-xiang. Thermal conductivity of aluminum alloys—A review [J]. Materials, 2023, 16: 2972.

[33] WANG Kai-xian, YIN Deng-feng, ZHAO Ying-chao, ATRENS A, ZHAO Ming-chun. Microstructural evolution upon heat treatments and its effect on corrosion in Al−Zn−Mg alloys containing Sc and Zr [J]. Journal of Materials Research and Technology, 2020, 9: 5077−5089.

[34] YING Tao, CHI Hang, ZHENG Ming-yi, LI Zi-tong, UHER C. Low-temperature electrical resistivity and thermal conductivity of binary magnesium alloys [J]. Acta Materialia, 2014, 80: 288−295.

[35] QI Fu-gang, ZHANG Ding-fei, ZHANG Xiao-hua, PAN Fu-sheng. Effect of Y addition on microstructure and mechanical properties of Mg−Zn−Mn alloy [J]. Transactions of Nonferrous Metals Society of China, 2014, 24: 1352−1364.

[36] XIE Tian-ci, SHI Hui, WANG Hong-bin, LUO Qun, LI Qian, CHOU Kuo-Chih. Thermodynamic prediction of thermal diffusivity and thermal conductivity in Mg−Zn−La/Ce system [J]. Journal of Materials Science and Technology, 2022, 97: 147−155.

[37] HUANG Xin-sheng, BIAN Ming-zhe, NAKATSUGAWA I, CHINO Y, SATO M, YAMAZAKI K, KIDO F, UEDA H, INOUE M. Simultaneously achieving excellent mechanical properties and high thermal conductivity in a high Mn-containing Mg−Zn−Ca−Al−Mn sheet alloy [J]. Journal of Alloys and Compounds, 2021, 887: 161394.

热压缩同步提高挤压 Mg−Mn−Zn 合金的强度和热导率

刘海峰[1]，杨续跃[1]，张宇修[1]，Hiromi NAGAUMI[2]，赵明纯[1]，石智勇[1]，Andrej ATRENS[3]

1. 中南大学 材料科学与工程学院，长沙 410083；

2. 苏州大学 钢铁学院，苏州 215100；

3. School of Mechanical & Mining Engineering, University of Queensland, Brisbane QLD4072, Australia

摘　要：对低含量挤压态 Mg−Mn−Zn 合金实施二次热压缩处理。合金首先在 150 ℃下以 15:1 的挤压比进行挤压加工，随后沿挤压方向在 180 ℃下进行真应变为 0.9 的热压缩处理。通过光学显微镜(OM)、扫描电子显微镜(SEM)、电子背散射衍射(EBSD)及透射电子显微镜(TEM)系统表征挤压态与热压缩态合金的显微组织、力学性能及热导率变化规律。该工艺通过实现显微组织均匀细化的同时,有效降低基面织构强度，成功实现材料强度与热导率的协同提高。结果表明：屈服强度(YS)、极限抗拉强度(UTS)和伸长率(EL)分别显著提升 77%、53%和 10%，同时热导率从 111 W/(m·K)提高至 125 W/(m·K)。该研究揭示了附加热压缩过程中多尺度组织结构演变与性能提升的内在关联机制，为开发兼具优异力学性能和热导率的新型镁合金提供了理论依据与技术途径。

关键词：镁合金；热压缩；强度；热导率

(Edited by Xiang-qun LI)